PHYSICAL REVIEW B **88**, 214403 (2013)

# Separation of longitudinal spin Seebeck effect from anomalous Nernst effect: Determination of origin of transverse thermoelectric voltage in metal/insulator junctions

T. Kikkawa,[1] K. Uchida,[1,2,*] S. Daimon,[1] Y. Shiomi,[1] H. Adachi,[3,4] Z. Qiu,[5]
D. Hou,[5] X.-F. Jin,[6] S. Maekawa,[3,4] and E. Saitoh[1,3,4,5]
[1]*Institute for Materials Research, Tohoku University, Sendai 980-8577, Japan*
[2]*PRESTO, Japan Science and Technology Agency, Saitama 332-0012, Japan*
[3]*Advanced Science Research Center, Japan Atomic Energy Agency, Tokai 319-1195, Japan*
[4]*CREST, Japan Science and Technology Agency, Tokyo 102-0076, Japan*
[5]*WPI Advanced Institute for Materials Research, Tohoku University, Sendai 980-8577, Japan*
[6]*State Key Laboratory of Surface Physics and Department of Physics, Fudan University, Shanghai 200433, China*
(Received 21 September 2013; published 6 December 2013)

The longitudinal spin Seebeck effect (LSSE) and the anomalous Nernst effect (ANE) are investigated in various metal/insulator junction systems and a clear separation of the LSSE from the ANE induced by static magnetic proximity is demonstrated. This separation is realized by comparing transverse thermoelectric voltage in in-plane magnetized (IM) and perpendicularly magnetized (PM) configurations, where the LSSE appears only in the IM configuration while the ANE appears both in the IM and PM configurations. We show that, in Pt/$Y_3Fe_5O_{12}$ samples, the LSSE voltage in the IM configuration is three orders of magnitude greater than the proximity-ANE contamination estimated from the data in the PM configuration. This quantitative voltage comparison between the IM and PM configurations is corroborated by systematic voltage measurements in $Ni_{81}Fe_{19}$/$Gd_3Ga_5O_{12}$, Pt/$Gd_3Ga_5O_{12}$, Au/$Y_3Fe_5O_{12}$, and Au/$Gd_3Ga_5O_{12}$ samples and by our phenomenological model calculation. The LSSE measurements in high magnetic field regions further confirm that the observed voltage in the Pt/$Y_3Fe_5O_{12}$ and Au/$Y_3Fe_5O_{12}$ samples is of magnon origin. We apply this voltage comparison method also to a $Ni_{81}Fe_{19}$/$Y_3Fe_5O_{12}$ sample and show that both the LSSE and ANE exist in this sample.

DOI: 10.1103/PhysRevB.88.214403 PACS number(s): 85.75.−d, 72.25.−b, 72.15.Jf, 73.50.Lw

## I. INTRODUCTION

In the field of spintronics,[1–4] many experimental and theoretical studies have been focused on spin-transport phenomena in paramagnet/ferromagnet junction systems, where a spin current[5,6] plays a central role. After the first demonstration of spin transport in insulator-based systems,[7] the Pt/$Y_3Fe_5O_{12}$ (YIG) junction system has become one of the prototype samples. In this system, itinerant spins in Pt and localized magnetic moments in YIG interact with each other via the interface *s*-*d* interaction (i.e., the spin-mixing conductance);[7,8] this interaction is the basic mechanism underlying various spin-current-related phenomena, such as spin pumping,[7–14] the spin Seebeck effect (SSE),[15–43] and spin Hall magnetoresistance (SMR).[44–49] However, in this Pt/YIG system, since Pt is near the Stoner ferromagnetic instability,[50,51] ferromagnetism may be induced in the Pt layer in the vicinity of the Pt/YIG interface due to a static magnetic proximity effect.[52] In fact, when the thickness of Pt is very thin (<3 nm), weak ferromagnetic signals were observed by means of x-ray magnetic circular dichroism (XMCD) measurements.[53,54] If the proximity ferromagnetism affects electron transport in the Pt layer, the signal due to the spin-current-related phenomena in the Pt/YIG system may be contaminated by the static magnetic proximity in the Pt layer. Therefore, an exclusive establishment of spin-current-related phenomena and the separation of them from the proximity ferromagnetism are important tasks in investigating electrical and thermal spin-transport phenomena.

In electrical transport in the Pt/YIG system, the spin-current mechanism has been shown to play a key role by extensive studies on SMR.[44–49] As recently demonstrated by many research groups, the Pt/YIG system exhibits a magnetoresistance effect; in spite of YIG being a very good electrical insulator, the resistance of the Pt layer reflects its magnetization direction. The experimental results show that magnetoresistance in the Pt/YIG system persists even when a nonmagnetic metal is inserted between Pt and YIG, excluding the contribution of proximity ferromagnetism in the Pt layer. Furthermore, the magnetic-field-angle dependence of magnetoresistance in the Pt/YIG system was found to be different from that of conventional anisotropic magnetoresistance in ferromagnetic conductors. The observed field-angle-dependent data are completely consistent with the SMR model[44] based on a combination of direct and inverse spin Hall effects,[12–14,55,56] indicating that the contribution from conventional anisotropic magnetoresistance due to static proximity ferromagnetism in Pt is negligibly small in the Pt/YIG system.

In thermal transport in the Pt/YIG system, the separation of the SSE from the anomalous Nernst effect (ANE)[57–62] is essential. If static proximity ferromagnetism in the Pt layer induces the ANE, the SSE signal in the Pt/YIG system may be contaminated by the proximity ANE, since the SSE in the longitudinal configuration [the longitudinal spin Seebeck effect (LSSE)][20,28] and the ANE have a similar configuration (see Sec. II and note that no ANE exists in the YIG layer since YIG is a very good insulator). In a recent Letter,[34] we have proposed and demonstrated a method for the exclusive detection of the LSSE; we have shown that the LSSE in the Pt/YIG system can be distinguished from the ANE by comparing the thermoelectric voltage in different magnetization and temperature-gradient configurations, and that the ANE contamination is negligibly small in this system, irrespective of whether or not proximity ferromagnetism exists in Pt.

In this paper, we report systematic experiments on the LSSE and ANE in the Pt/YIG, Pt/$Gd_3Ga_5O_{12}$ (GGG), Au/YIG, Au/GGG, $Ni_{81}Fe_{19}$/YIG, and $Ni_{81}Fe_{19}$/GGG systems and estimate possible ANE contamination in the Pt/YIG sample using both the experimental results and a phenomenological model calculation. We also investigate the magnetic field dependence of the LSSE in high field regions to confirm the magnon origin of the LSSE. These results further buttress our conclusion that the LSSE provides a dominant contribution in the Pt/YIG sample.

This paper is organized as follows. In Sec. II, we explain the configurations for measuring the LSSE and ANE and the method for the separation between them, followed by details of the experimental procedures. In Sec. III, we report the systematic experimental results and analyses of the LSSE and Nernst effects in the Pt/YIG, Pt/GGG, Au/YIG, Au/GGG, $Ni_{81}Fe_{19}$/YIG, and $Ni_{81}Fe_{19}$/GGG samples. Here, the phenomenological model calculation for estimating the proximity-ANE contamination is provided in Sec. III B3. Section IV is devoted to a summary of the present study.

## II. EXPERIMENTAL CONFIGURATION AND PROCEDURE

Figure 1(a) shows a schematic illustration of the LSSE in a paramagnetic metal/ferrimagnetic insulator junction system used in the present study. The sample comprises a paramagnetic metal film fabricated on the top surface of a ferrimagnetic insulator slab. When a temperature gradient $\nabla T$ is applied over the insulator slab perpendicular to the metal/insulator interface, a spin voltage is thermally generated and it injects a spin current with a spatial direction $\mathbf{J}_s$ ($\parallel \nabla T$) and spin-polarization vector $\boldsymbol{\sigma}$ ($\parallel$ the magnetization $\mathbf{M}$ of the insulator) into the paramagnetic metal film. The spin current is converted into an electric field $\mathbf{E}_{\mathrm{ISHE}}$ by the inverse spin Hall effect (ISHE)[12–14,55,56] in the metal [see Fig. 1(a)]. When $\mathbf{M}$ is along the $x$ direction, $\mathbf{E}_{\mathrm{ISHE}}$ is generated in the paramagnetic metal film along the $y$ direction according to the relation

$$\mathbf{E}_{\mathrm{ISHE}} = \frac{\theta_{\mathrm{SH}}\rho}{A}\left(\frac{2e}{\hbar}\right)\mathbf{J}_s \times \boldsymbol{\sigma}, \tag{1}$$

where $\theta_{\mathrm{SH}}$, $\rho$, $A$, $e$, and $\hbar$ are the spin Hall angle, electrical resistivity of the metal, contact area of the metal/insulator interface, electron charge, and Planck constant divided by $2\pi$, respectively. Therefore, by measuring $\mathbf{E}_{\mathrm{ISHE}}$ in the paramagnetic metal film, one can detect the LSSE electrically. Here, the use of a highly resistive insulator, such as YIG, is indispensable to the LSSE experiments to eliminate artifacts caused by electric conduction in the ferrimagnetic insulator.

Figure 1(b) shows a schematic illustration of the ANE in a ferromagnetic conductor. When $\nabla T$ is applied to a ferromagnetic conductor perpendicular to the $\mathbf{M}$ direction, an electric field is induced by the ANE according to the relation

$$\mathbf{E}_{\mathrm{ANE}} = S_{\mathrm{ANE}} \nabla T \times \mathbf{m}, \tag{2}$$

where $S_{\mathrm{ANE}}$ is the anomalous Nernst coefficient, which is typically proportional to the magnetization of the ferromagnet,[58] and $\mathbf{m}$ is the unit vector of magnetization ($\mathbf{m} = \mathbf{M}/|\mathbf{M}|$). Equation (2) means that, when $\nabla T \parallel z$ and $\mathbf{M} \| x$, $\mathbf{E}_{\mathrm{ANE}}$ is generated along the $y$ direction, a configuration similar to that of the LSSE [compare Figs. 1(a) and 1(b)]. Therefore, in the Pt/YIG system, although the ANE in YIG does not exist at

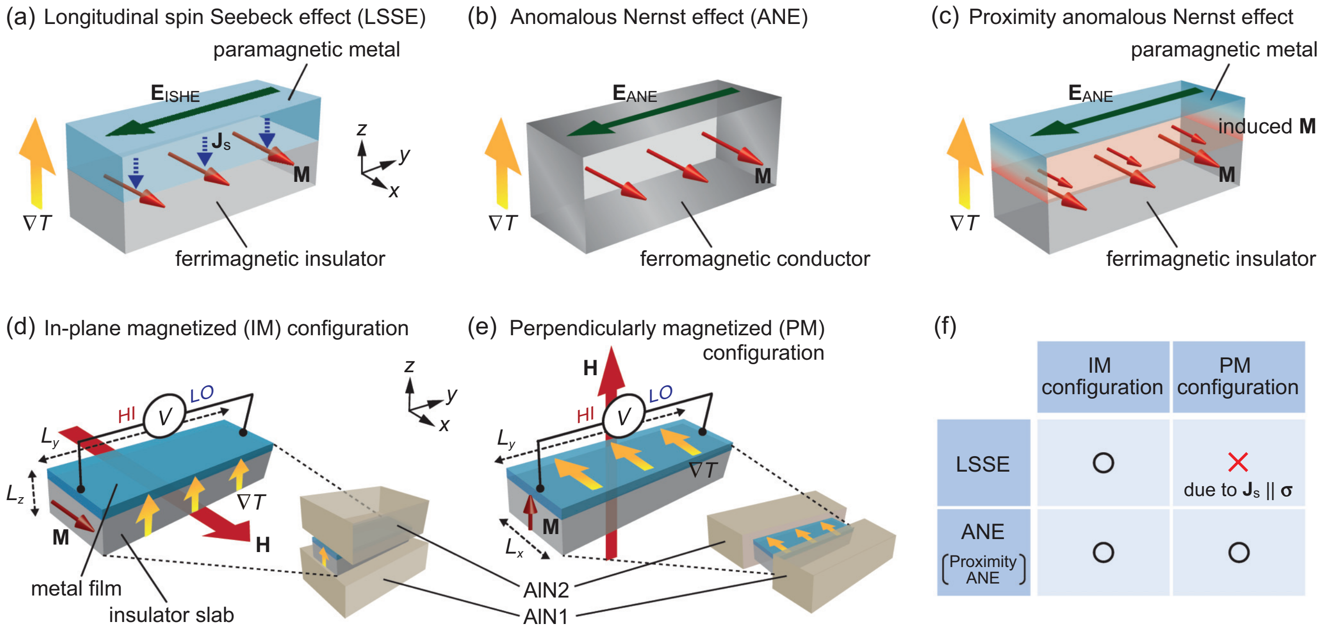

FIG. 1. (Color online) Schematic illustrations of the (a) LSSE, (b) ANE, and (c) proximity ANE. Schematic illustrations of the (d) IM and (e) PM configurations. $\nabla T$, $\mathbf{H}$, $\mathbf{M}$, $\mathbf{E}_{\mathrm{ISHE}}$ ($\mathbf{E}_{\mathrm{ANE}}$), and $\mathbf{J}_s$ denote the temperature gradient, magnetic field (with magnitude $H$), magnetization vector, electric field induced by the ISHE (ANE), and spatial direction of the thermally generated spin current, respectively. $L_y$, $L_x$, and $L_z$ denote the length, width, and thickness of the sample, respectively. (f) LSSE and ANE in the IM and PM configurations. The LSSE voltage disappears in the PM configuration due to the ISHE symmetry, while the (proximity) ANE voltage can appear in both the configurations.

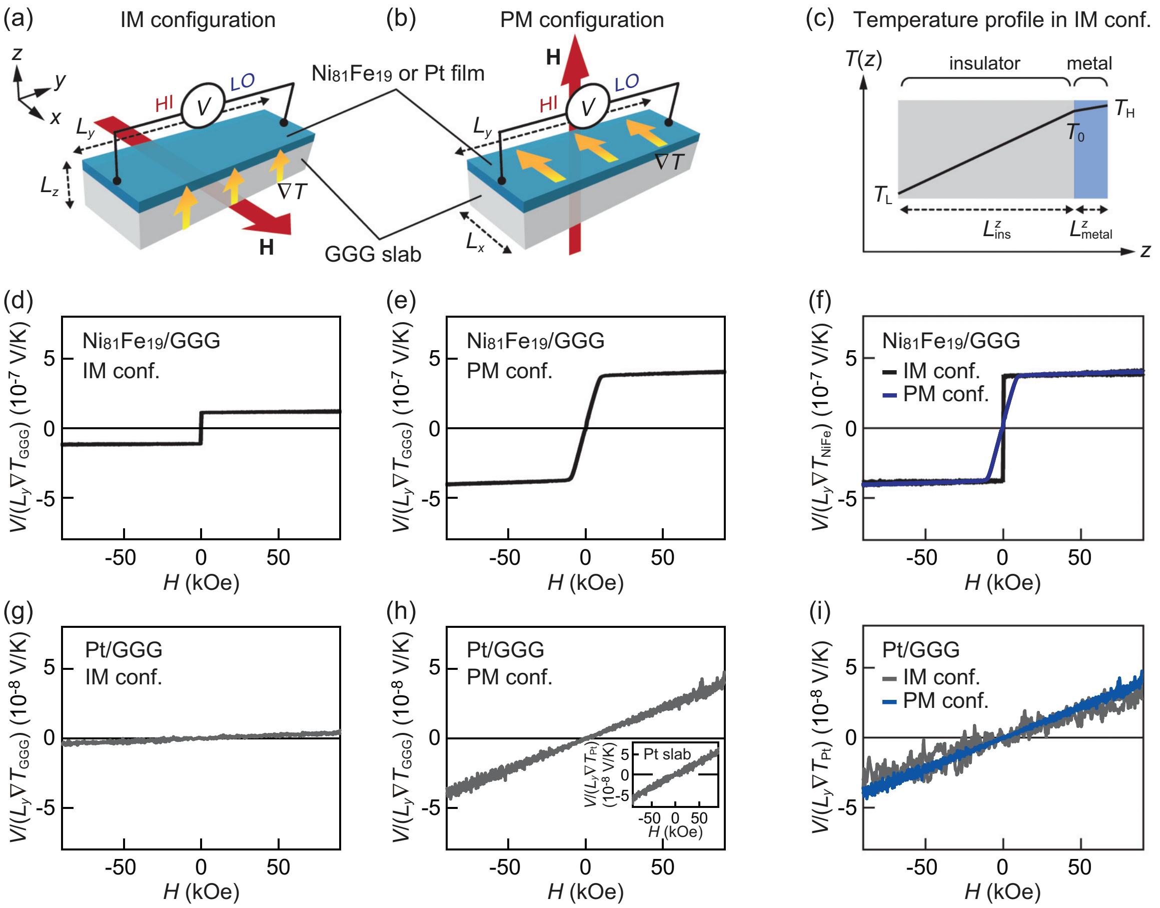

FIG. 2. (Color online) Schematic illustrations of the $Ni_{81}Fe_{19}$/GGG or Pt/GGG sample in the (a) IM and (b) PM configurations. (c) Temperature profile in the metal-film/insulator-slab junction system in the IM configuration along the $z$ direction. $T_{\mathrm{H}}$, $T_0$, and $T_{\mathrm{L}}$ denote the temperature at the top surface of the metal film, at the interface, and at the bottom surface of the insulator slab. $L^z_{\mathrm{ins(metal)}}$ is the thickness of the insulator (metal), where $L^z_{\mathrm{metal}} \ll L^z_{\mathrm{ins}} \sim L_z$ in the present samples. $H$ dependence of $V/(L_y \nabla T_{\mathrm{GGG}})$ in the $Ni_{81}Fe_{19}$/GGG sample in the (d) IM and (e) PM configurations. (f) $H$ dependence of $V/(L_y \nabla T_{\mathrm{NiFe}})$ in the $Ni_{81}Fe_{19}$/GGG sample in the IM and PM configurations. $H$ dependence of $V/(L_y \nabla T_{\mathrm{GGG}})$ in the Pt/GGG sample in the (g) IM and (h) PM configurations. The inset to (h) shows the $H$ dependence of $V/(L_y \nabla T_{\mathrm{Pt}})$ in the Pt plate in the PM configuration. (i) $H$ dependence of $V/(L_y \nabla T_{\mathrm{Pt}})$ in the Pt/GGG sample in the IM and PM configurations. $\nabla T_{\mathrm{GGG}}$, $\nabla T_{\mathrm{NiFe}}$, and $\nabla T_{\mathrm{Pt}}$ denote the temperature gradient in the GGG substrate, $Ni_{81}Fe_{19}$ film, and Pt film, respectively.

all, the ANE in the Pt layer may contaminate the LSSE if static proximity ferromagnetism in Pt induces the ANE [see Fig. 1(c)].

To realize the exclusive detection of the LSSE in the Pt/YIG system, it is important to separate the spin-current-induced signal from the ANE signal. We found that the LSSE in the Pt/YIG system can be separated from the ANE by comparing the transverse thermoelectric voltage in an in-plane magnetized (IM) configuration (the LSSE setup) and a perpendicularly magnetized (PM) configuration.[34] Here, in the IM (PM) configuration, an external magnetic field **H** is applied parallel (perpendicular) to the Pt/YIG interface and a temperature gradient is applied perpendicular (parallel) to the interface [see Figs. 1(d) and 1(e)]. In the PM configuration, the ANE signal can appear since the temperature gradient, magnetization, and interelectrode direction are at right angles to one another [see Eq. (2)], while the LSSE signal should disappear due to the symmetry of the ISHE [see Eq. (1) and note that $\mathbf{J}_{\mathrm{s}} \parallel \boldsymbol{\sigma}$ in the PM configuration]. Therefore, a quantitative comparison of the voltage between these configurations enables the estimation of ANE contamination in the Pt/YIG system [see Fig. 1(f)]. Here we note that, in the PM configuration, even a possible tiny temperature gradient perpendicular to the Pt-film plane[25,60] does not affect the voltage signal, since a Nernst voltage is not generated due to the collinear orientation of the perpendicular temperature gradient and the magnetization (or the magnetic field).

In this paper, to comprehensively investigate the LSSE and ANE in metal/insulator junction systems, we compare the transverse thermoelectric voltage between the IM and PM configurations not only in the Pt/YIG system but also in the Pt/GGG, Au/YIG, Au/GGG, $Ni_{81}Fe_{19}$/YIG, and $Ni_{81}Fe_{19}$/GGG systems. The sample consists of a Pt, Au, or $Ni_{81}Fe_{19}$ thin film fabricated on a single-crystalline ferrimagnetic YIG or paramagnetic GGG slab. The Pt, Au, or $Ni_{81}Fe_{19}$ film was deposited on the entire (111) surface of the YIG or GGG slab. The length ($L_y$), width ($L_x$), and thickness ($L_z$) of the YIG and GGG slabs are 6.0, 2.0, and 1.0 mm, respectively. The thickness of the Pt, Au, and $Ni_{81}Fe_{19}$ films is 10 nm except when collecting thickness-dependent data in Sec. III B2. Both in the IM and PM configurations, the sample was sandwiched between two AlN plates with a high thermal conductivity (~160 W/mK) [see Figs. 1(d) and 1(e)]; AlN1 (AlN2) is thermally connected to a heat bath (a ceramic heater), where the temperature of the heat bath is stabilized at $T_{\mathrm{L}} = 300$ K. By applying a charge current to the ceramic heater, the temperature of the AlN2 plate is stabilized at $T_{\mathrm{H}} = 300\ \mathrm{K} + \Delta T$, where the temperature difference $\Delta T$ between the AlN1 and AlN2 plates was measured with E-type thermocouples. To apply a uniform temperature gradient to the sample in the PM configuration, both the metal film (Pt, Au, or $\mathrm{Ni_{81}Fe_{19}}$) and the insulator slab (YIG or GGG) are thermally well connected to the AlN plates with thermal grease. In the IM (PM) configuration, we measured an electric voltage difference $V$ between the end of the Pt, Au, or $\mathrm{Ni_{81}Fe_{19}}$ film along the $y$ direction by applying $\nabla T$ along the $z$ ($x$) direction and $\mathbf{H}$ (with magnitude $H$) along the $x$ ($z$) direction [see Figs. 1(d) and 1(e)].

## III. RESULTS AND DISCUSSION

### A. $\mathrm{Ni_{81}Fe_{19}}$/GGG and Pt/GGG sample systems

In this section, by measuring the transverse thermoelectric voltage in the $\mathrm{Ni_{81}Fe_{19}}$/GGG and Pt/GGG samples, we confirm the temperature-gradient distributions in the IM and PM configurations and show that the $\mathrm{Ni_{81}Fe_{19}}$ and Pt films exhibit isotropic Nernst effects in these configurations. These results ensure the validity of the voltage comparison between the IM and PM configurations.

Figures 2(d) and 2(e) respectively show the transverse thermopower as a function of $H$ in the IM and PM configurations for the $\mathrm{Ni_{81}Fe_{19}}$/GGG sample, where only the ANE (and a small normal Nernst effect) exists. Here, the vertical axes are normalized by geometric factors to quantitatively compare the signals between the IM and PM configurations, $V/(L_y \nabla T_{\mathrm{GGG}})$ with $\nabla T_{\mathrm{GGG}} = \Delta T/L_z$ ($\nabla T_{\mathrm{GGG}} = \Delta T/L_x$) being the temperature gradient in the GGG substrate in the IM (PM) configuration. In both configurations, the $\mathrm{Ni_{81}Fe_{19}}$/GGG sample exhibits a clear voltage signal whose sign is reversed when $\mathbf{H}$ is reversed. This voltage signal is attributed to the ANE since no LSSE voltage is generated in the plain $\mathrm{Ni_{81}Fe_{19}}$ film with no spin-current detector.

Importantly, in the $\mathrm{Ni_{81}Fe_{19}}$/GGG sample, the ANE voltage in the IM configuration is smaller than that in the PM configuration [see Figs. 2(d) and 2(e)]. This behavior is natural since the thermal conductivity of $\mathrm{Ni_{81}Fe_{19}}$ ($\kappa_{\mathrm{NiFe}}$) is greater than that of GGG ($\kappa_{\mathrm{GGG}}$); in the IM configuration, the temperature gradient in the $\mathrm{Ni_{81}Fe_{19}}$ film becomes smaller than that in the GGG slab due to the difference in the thermal conductivities [Fig. 2(c)], while the temperature gradient in the $\mathrm{Ni_{81}Fe_{19}}$ film is the same as that in the GGG slab in the PM configuration (note again that, in the PM configuration, both the $\mathrm{Ni_{81}Fe_{19}}$ film and the GGG slab are thermally connected to the AlN plates directly). The temperature-gradient distribution in the IM configuration can be estimated from a simple phenomenological calculation shown in Sec. III B3; by using $\kappa_{\mathrm{NiFe}} = 30$ W/mK and $\kappa_{\mathrm{GGG}} = 9.0$ W/mK,[63,64] the temperature gradient in the $\mathrm{Ni_{81}Fe_{19}}$ layer in the IM configuration is estimated to be $\nabla T_{\mathrm{NiFe}} = (\kappa_{\mathrm{GGG}}/\kappa_{\mathrm{NiFe}})\Delta T/L_z = 0.30\nabla T_{\mathrm{GGG}}$. By normalizing the observed voltage with the temperature gradient in the $\mathrm{Ni_{81}Fe_{19}}$ layer, the magnitude of the ANE signal in the IM configuration coincides with that in the PM configuration [Fig. 2(f)], confirming that the $\mathrm{Ni_{81}Fe_{19}}$ film on the GGG slab exhibits an isotropic ANE in these configurations.

We also performed similar experiments using the Pt/GGG sample, where only the normal Nernst effect exists. As shown

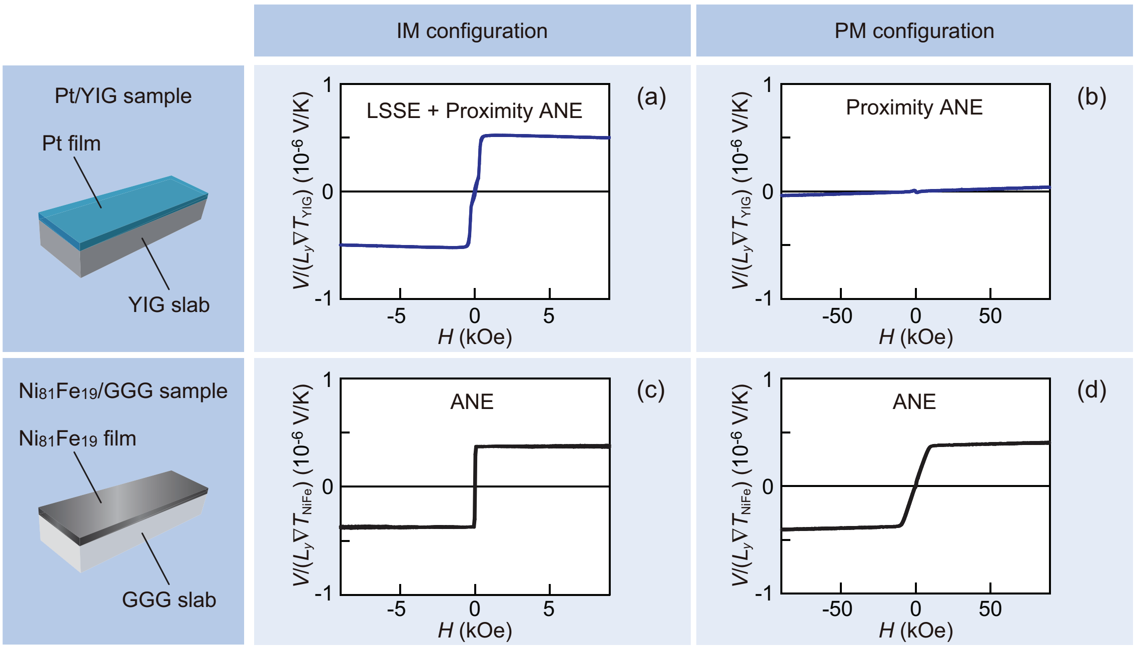

FIG. 3. (Color online) $H$ dependence of $V/(L_y \nabla T_{\mathrm{YIG}})$ in the Pt/YIG sample in the (a) IM and (b) PM configurations. $H$ dependence of $V/(L_y \nabla T_{\mathrm{NiFe}})$ in the $\mathrm{Ni_{81}Fe_{19}}$/GGG sample in the (c) IM and (d) PM configurations. $\nabla T_{\mathrm{YIG}}$ denotes the temperature gradient in the YIG substrate.

in Figs. 2(g) and 2(h), the voltage signal in the Pt/GGG sample varies linearly with respect to $H$ in both configurations due to the normal Nernst effect. Although the magnitude of the raw normal Nernst voltage in the IM configuration is also smaller than that in the PM configuration [Figs. 2(g) and 2(h)], the signals normalized by the temperature gradient in the Pt layer coincide with each other [Fig. 2(i)], where we use $\nabla T_{\mathrm{Pt}} = (\kappa_{\mathrm{GGG}}/\kappa_{\mathrm{Pt}})\Delta T/L_z = 0.125\nabla T_{\mathrm{GGG}}$ in the IM configuration based on $\kappa_{\mathrm{Pt}} = 72$ W/mK and $\kappa_{\mathrm{GGG}} = 9.0$ W/mK.[63,64] We also found that the normal Nernst coefficient in the Pt/GGG sample in the PM configuration is comparable to that in a Pt plate without a substrate [see the inset to Fig. 2(h)], confirming again that an in-plane temperature gradient is properly generated in the Pt film even in the presence of the substrate. The isotropic Nernst effects observed here verify the validity of the voltage comparison between the IM and PM configurations not only in the $\mathrm{Ni}_{81}\mathrm{Fe}_{19}$/GGG and Pt/GGG samples but also in the Pt/YIG sample that is discussed below.

### B. Pt/YIG sample system

#### 1. Comparison of voltage between IM and PM configurations

Now we are in a position to demonstrate the comparison of the voltage signals in the Pt/YIG sample between the IM and PM configurations. In Figs. 3(a) and 3(b), we show the transverse thermopower $V/(L_y\nabla T_{\mathrm{YIG}})$ in the Pt/YIG sample as a function of $H$ in both configurations. The thermopower in the IM configuration was found to be much greater than that in the PM configuration. Here, the magnitude of the normal Nernst voltage in the Pt/YIG sample in the PM configuration is comparable to that in the Pt/GGG sample and the plain Pt plate, confirming that the in-plane temperature gradient is generated in the Pt/YIG sample in the PM configuration. The voltage behavior in the Pt/YIG sample is completely different from that in the $\mathrm{Ni}_{81}\mathrm{Fe}_{19}$/GGG sample, where a clear ANE voltage appears in both the IM and PM configurations (see Fig. 3).

To check the influence of possible nonuniform temperature gradients that are perpendicular to the Pt/YIG interface in the PM configuration, we performed the same measurements using a Pt wire/YIG sample in which the Pt film is replaced with multiple thin Pt wires. Here, we formed three Pt wires with a width of 0.1 mm and a thickness of 10 nm on the top surface of the YIG slab at the intervals of 0.6 mm [see Figs. 4(a) and 4(b)]. As shown in Figs. 4(c) and 4(d), we observed the same behavior also in this Pt wire/YIG sample; the large voltage signals and small normal Nernst signals appear in the Pt wires in the IM and PM configurations, respectively. Importantly, the voltage behavior in the Pt wire/YIG sample does not depend on the Pt-wire position, indicating that the possible nonuniform temperature gradients in the PM configuration are irrelevant to the observed voltage signals. These experimental results confirm again that, in the Pt/YIG samples, the transverse thermoelectric voltage in the IM configuration is much greater than that in the PM configuration.

The above results clearly show that the transverse thermoelectric voltage in the Pt/YIG sample is dominated by the ISHE voltage induced by the LSSE and that the proximity-ANE contamination is negligibly small. Since only the ANE appears in the PM configuration [Fig. 1(f)], we can estimate the magnitude of the proximity ANE in the Pt/YIG sample from the data shown in Fig. 3(b), where the ANE thermopower $V_{\mathrm{ANE}}/(L_y\nabla T_{\mathrm{YIG}})$ is extracted by extrapolating the $V/(L_y\nabla T_{\mathrm{YIG}})$ data in the high field region (20 kOe $< H <$ 90 kOe) to zero field. We obtain a finite but small ANE contribution from the voltage data in the PM configuration; the proximity-ANE thermopower is estimated to be $V_{\mathrm{ANE}}/(L_y\nabla T_{\mathrm{YIG}}) = 0.003\ \mu$V/K for the Pt/YIG sample with $L_{\mathrm{Pt}}^z = 10$ nm. This proximity-ANE contribution is further reduced to $0.0003\ \mu$V/K in the IM configuration owing to the high thermal conductivity of Pt (see Fig. 2 and Sec. III B3). Therefore, by combining this ANE thermopower and the voltage data in the IM configuration, the LSSE thermopower in the Pt/YIG sample with $L_{\mathrm{Pt}}^z = 10$ nm is estimated to be $V_{\mathrm{LSSE}}/(L_y\nabla T_{\mathrm{YIG}}) = 0.521\ \mu$V/K, showing that the LSSE contribution is more than three orders of magnitude greater than the proximity-ANE contamination.

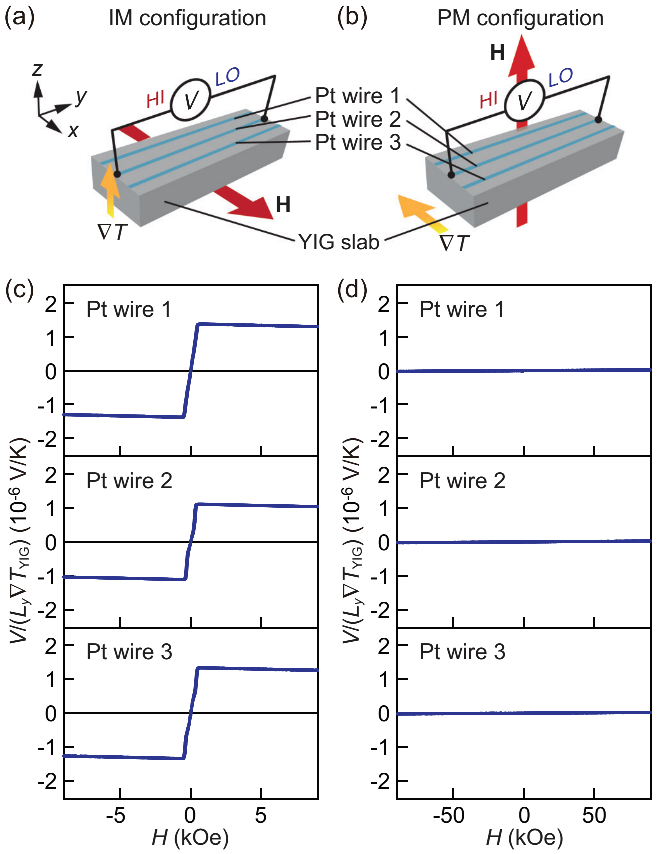

FIG. 4. (Color online) Schematic illustrations of the Pt wire /YIG sample in the (a) IM and (b) PM configurations. $H$ dependence of $V/(L_y\nabla T_{\mathrm{YIG}})$ in the Pt wire /YIG sample in the (c) IM and (d) PM configurations.

#### 2. Pt thickness dependence

Here, we investigate the Pt thickness dependence of the transverse thermoelectric voltage in the Pt/YIG samples. In Figs. 5(a) and 5(b), we show the $H$ dependence of $V/(L_y\nabla T_{\mathrm{YIG}})$ in the Pt/YIG samples for various values of the Pt thickness ($L_{\mathrm{Pt}}^z = 1.5$, 3, 10, 24 nm) in the IM and PM configurations, respectively. The LSSE thermopower in the IM configuration monotonically increases with decreasing $L_{\mathrm{Pt}}^z$, consistent with previous results.[33] Importantly, the LSSE

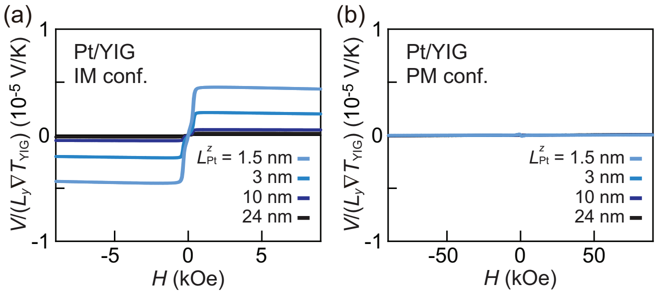

FIG. 5. (Color online) $H$ dependence of $V/(L_y\nabla T_{\mathrm{YIG}})$ in the Pt/YIG samples for various values of the Pt thickness $L^z_{\mathrm{Pt}}$ in the (a) IM and (b) PM configurations.

thermopower is much greater than the proximity-ANE thermopower in all the Pt/YIG samples, even when the thickness of the Pt film is very thin. Although ferromagnetic characteristics were observed in very thin ($<3$ nm) Pt films on YIG by means of XMCD measurements,[53,54] the experimental results shown here confirm that the LSSE provides a dominant contribution in the Pt/YIG samples, irrespective of whether or not the proximity ferromagnetism exists in Pt (see also Sec. III B3).

### *3. Estimation of proximity ANE using a model calculation*

In this section, we estimate the proximity-ANE contamination in the Pt/YIG sample using a phenomenological model calculation. To discuss the ANE induced by static proximity ferromagnetism near the Pt/YIG interface, it is important to consider the short-circuit effect[65] in the Pt layer, since proximity ferromagnetism in Pt is expected to exist only in several atomic layers adjacent to the interface and the remaining region is a paramagnetic metal with high electrical conductivity. To simplify this situation, in our model calculation, the Pt layer is divided into two parts: a proximity-induced ferromagnetic region near the Pt/YIG interface and a paramagnetic region [see Fig. 6(a)].[36] Hereafter, the ferromagnetic and paramagnetic regions of the Pt layer are labeled by the indexes I and II, respectively, and the thicknesses of these regions are defined as $L^z_{\mathrm{Pt(I)}}$ and $L^z_{\mathrm{Pt(II)}}$, where the total Pt thickness is $L^z_{\mathrm{Pt}} = L^z_{\mathrm{Pt(I)}} + L^z_{\mathrm{Pt(II)}}$. In the following model calculation, to estimate the contribution from the proximity ANE, we consider the situation where the transverse thermoelectric voltage is generated only in the Pt(I) layer.

In the linear-response region, the charge-current density $\mathbf{J}$ is given by

$$\mathbf{J} = \boldsymbol{\sigma}\mathbf{E} - \boldsymbol{\alpha}\nabla T, \tag{3}$$

where $\mathbf{E}$, $\boldsymbol{\sigma}$, and $\boldsymbol{\alpha}$ are the electric field, electrical conductivity tensor, and Peltier tensor, respectively.[50] In the IM configuration shown in Fig. 6(a), Eq. (3) can be rewritten as

$$\begin{aligned} J^y_{\mathrm{I}} &= \sigma^{yy}E^y + \sigma^{yz}E^z - \alpha^{yz}\nabla_z T_{\mathrm{Pt}},\\ J^z_{\mathrm{I}} &= \sigma^{zy}E^y + \sigma^{zz}E^z - \alpha^{zz}\nabla_z T_{\mathrm{Pt}},\\ J^y_{\mathrm{II}} &= \sigma^{yy}E^y,\\ J^z_{\mathrm{II}} &= \sigma^{zz}E^z - \alpha^{zz}\nabla_z T_{\mathrm{Pt}}. \end{aligned} \tag{4}$$

Here, we consider the open-circuit condition $I^y = (L_x L^z_{\mathrm{Pt(I)}})J^y_{\mathrm{I}} + (L_x L^z_{\mathrm{Pt(II)}})J^y_{\mathrm{II}} = 0$ and $I^z = (L_x L_y)J^z_{\mathrm{I}} = (L_x L_y)J^z_{\mathrm{II}} = 0$, where $I^y$ ($I^z$) is the charge current along the $y$ ($z$) direction and $L_x$ ($L_y$) is the length of the Pt film along the $x$ ($y$) direction [see Fig. 6(a)]. Under this condition, the electric field in the Pt film along the $y$ direction is described as

$$E^y = \left(\frac{L^z_{\mathrm{Pt(I)}}}{L^z_{\mathrm{Pt}}}\right) S^{\mathrm{ANE}}_{\mathrm{Pt(I)}} \nabla_z T_{\mathrm{Pt}}, \tag{5}$$

where the factor $L^z_{\mathrm{Pt(I)}}/L^z_{\mathrm{Pt}}$ comes from the short-circuit effect that reduces the output voltage in the Pt film and $S^{\mathrm{ANE}}_{\mathrm{Pt(I)}} = (1/\sigma^{yy})[\alpha^{yz} - (\sigma^{yz}/\sigma^{yy})\alpha^{yy}]$ is the proximity-ANE coefficient in the Pt(I) layer.

To estimate the proximity-ANE contribution and to compare it with the experimental results, we need to know the temperature-gradient distribution in the Pt/YIG sample in the IM configuration, i.e., the relation between $\nabla_z T_{\mathrm{Pt}}$ and $\nabla_z T_{\mathrm{YIG}}$. Since the heat-current conservation across the Pt/YIG interface gives the relation $-\kappa_{\mathrm{Pt}}(T_{\mathrm{H}} - T_0)/L^z_{\mathrm{Pt}} = -\kappa_{\mathrm{YIG}}(T_0 - T_{\mathrm{L}})/L^z_{\mathrm{YIG}}$, the temperature gradient in the Pt layer along the $z$

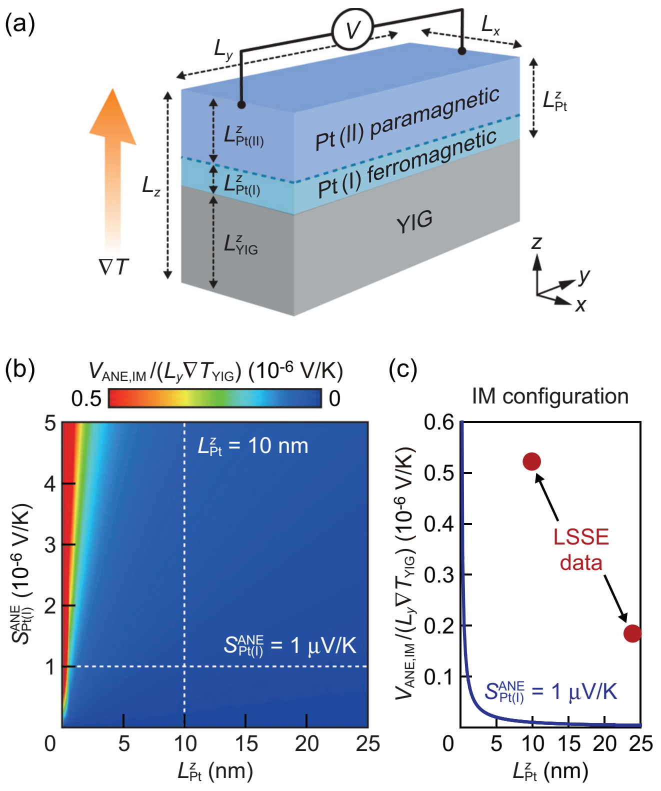

FIG. 6. (Color online) (a) A schematic illustration of the Pt/YIG sample for the estimation of the proximity-ANE contribution in the IM configuration. (b) Contour plot of the proximity-ANE thermopower $V_{\mathrm{ANE,IM}}/(L_y\nabla_z T_{\mathrm{YIG}})$ as functions of $L^z_{\mathrm{Pt}}$ and $S^{\mathrm{ANE}}_{\mathrm{Pt(I)}}$ in the IM configuration, calculated from Eq. (7) with $L^z_{\mathrm{Pt(I)}} = 1$ nm. (c) $L^z_{\mathrm{Pt}}$ dependence of $V_{\mathrm{ANE,IM}}/(L_y\nabla_z T_{\mathrm{YIG}})$ at $S^{\mathrm{ANE}}_{\mathrm{Pt(I)}} = 1\mu$ V/K, calculated from Eq. (7) with $L^z_{\mathrm{Pt(I)}} = 1$ nm. The red circle data points are the observed LSSE thermopower in the Pt/YIG samples with $L^z_{\mathrm{Pt}} = 10$ and 24 nm. The LSSE signals in the Pt/YIG samples with $L^z_{\mathrm{Pt}} = 1.5$ and 3 nm are, respectively, $V_{\mathrm{LSSE}}/(L_y\nabla T_{\mathrm{YIG}}) = 4.473$ and 2.186 $\mu$V/K [see Fig. 5(a)], much greater than the maximum value of the vertical axis.

direction becomes

$$\nabla_z T_{\mathrm{Pt}} = \frac{T_{\mathrm{H}} - T_0}{L^z_{\mathrm{Pt}}} = \left(\frac{\kappa_{\mathrm{YIG}}}{\kappa_{\mathrm{Pt}}}\right)\frac{\Delta T}{L^z_{\mathrm{YIG}}} = \left(\frac{\kappa_{\mathrm{YIG}}}{\kappa_{\mathrm{Pt}}}\right)\nabla_z T_{\mathrm{YIG}} \quad (6)$$

because of $L^z_{\mathrm{Pt}} \ll L^z_{\mathrm{YIG}}$, where $T_0$ is the temperature at the interface and $\Delta T = T_{\mathrm{H}} - T_{\mathrm{L}}$ [see Fig. 2(c)]. Making use of $\kappa_{\mathrm{Pt}} =$ 72 W/mK and $\kappa_{\mathrm{YIG}} = 7.4$ W/mK,[63,64] we obtain $\nabla_z T_{\mathrm{Pt}} = 0.10\nabla_z T_{\mathrm{YIG}}$ at room temperature. This estimation is corroborated by the Nernst measurements in the $\mathrm{Ni}_{81}\mathrm{Fe}_{19}$/GGG and Pt/GGG samples shown in Fig. 2. By combining this relation with Eq. (5), the transverse thermopower induced by the proximity ANE in the Pt/YIG sample is expressed as

$$\frac{V_{\mathrm{ANE,IM}}}{L_y \nabla_z T_{\mathrm{YIG}}} = 0.10\left(\frac{L^z_{\mathrm{Pt(I)}}}{L^z_{\mathrm{Pt}}}\right) S^{\mathrm{ANE}}_{\mathrm{Pt(I)}} \quad (7)$$

in the IM configuration, where $V_{\mathrm{ANE,IM}} = E^y L_y$. Note that, since $\nabla_x T_{\mathrm{YIG}} = \nabla_x T_{\mathrm{Pt}}$ in the PM configuration, the proximity-ANE thermopower in the PM configuration is expressed as $V_{\mathrm{ANE,PM}}/(L_y \nabla_x T_{\mathrm{YIG}}) = (L^z_{\mathrm{Pt(I)}}/L^z_{\mathrm{Pt}}) S^{\mathrm{ANE}}_{\mathrm{Pt(I)}}$.

Equation (7) enables the estimation of the proximity-ANE thermopower in the IM configuration. In Fig. 6(b), we show the contour plot of $V_{\mathrm{ANE,IM}}/(L_y \nabla_z T_{\mathrm{YIG}})$ estimated from Eq. (7) as functions of $L^z_{\mathrm{Pt}}$ and $S^{\mathrm{ANE}}_{\mathrm{Pt(I)}}$, where the thickness of the Pt(I) layer is fixed at $L^z_{\mathrm{Pt(I)}} = 1$ nm.[33] For example, even when we assume the large proximity-ANE coefficient $S^{\mathrm{ANE}}_{\mathrm{Pt(I)}} = 1\ \mu$V/K in the Pt(I) layer, the output thermopower induced by the proximity ANE is reduced to $V_{\mathrm{ANE,IM}}/(L_y \nabla_z T_{\mathrm{YIG}}) = 0.01\ \mu$V/K in the Pt/YIG sample with $L^z_{\mathrm{Pt}} = 10$ nm due to the short-circuit effect and the high thermal conductivity of Pt, which is much smaller than the observed LSSE thermopower, $V_{\mathrm{LSSE}}/(L_y \nabla T_{\mathrm{YIG}}) = 0.521\ \mu$V/K [see Fig. 6(c)]. Here we note that $S^{\mathrm{ANE}}_{\mathrm{Pt(I)}} = 1\ \mu$V/K is larger than the ANE coefficient for FePt (∼0.7 $\mu$V/K),[62] a ferromagnetic metal with a large spin-orbit interaction. Since the induced magnetization in the Pt film on YIG (∼90 G)[66] is much smaller than the saturation magnetization of FePt (>10 kG)[67] and the ANE coefficient is proportional to the magnetization in general, the actual $S^{\mathrm{ANE}}_{\mathrm{Pt(I)}}$ value in the Pt(I) layer should be much smaller than 1 $\mu$V/K. In fact, when we substitute the proximity-ANE thermopower estimated from the data in Fig. 3(b) to Eq. (7), we obtain $S^{\mathrm{ANE}}_{\mathrm{Pt(I)}} = 0.03\ \mu$V/K in the Pt(I) layer. Therefore, the observed large thermoelectric voltage in the Pt/YIG sample can never be explained by the proximity ANE.

### *4. High field measurements in IM configuration*

Here we show that the LSSE and ANE can be distinguished also by measuring the transverse thermoelectric voltage in high magnetic field regions in the IM configuration. Figure 7(a) shows the $H$ dependence of $V/(L_y \nabla T_{\mathrm{YIG}})$ in the Pt/YIG sample in the IM configuration, measured when the magnetic field was swept between ±90 kOe. We found that the magnitude of the LSSE signal in the Pt/YIG sample gradually decreases with increasing the magnetic field after taking the maximum value, while the ANE is not suppressed under the high magnetic field [compare Figs. 7(a) and 7(b)]. The suppression of the voltage in the Pt/YIG sample is very small in low magnetic field regions [Fig. 7(c)] but reaches ∼30% of the maximum LSSE signal at $H = \pm 90$ kOe [Fig. 7(a)], a situation which cannot be explained also by the small normal Nernst effect in the Pt film [Fig. 7(b)]. This voltage suppression under the high magnetic field was observed to appear in the Pt/YIG samples, irrespective of the Pt thickness [see Figs. 7(e) and 7(f)]. This behavior is the exclusive feature of the LSSE that arises only when YIG is used as a substrate.

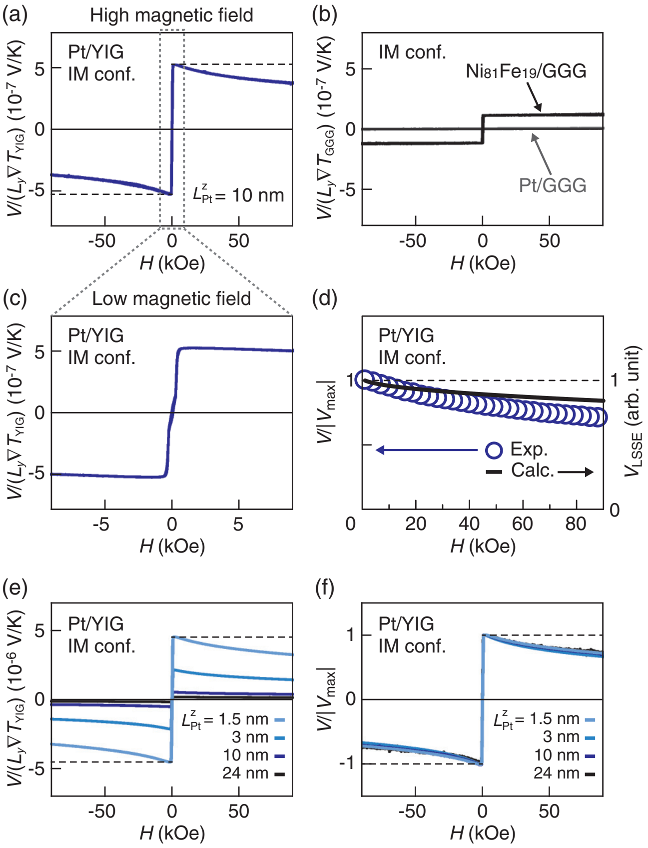

FIG. 7. (Color online) (a) $H$ dependence of $V/(L_y \nabla T_{\mathrm{YIG}})$ in the Pt/YIG sample with $L^z_{\mathrm{Pt}} = 10$ nm, measured when the magnetic field was swept between ±90 kOe. (b) $H$ dependence of $V/(L_y \nabla T_{\mathrm{GGG}})$ in the $\mathrm{Ni}_{81}\mathrm{Fe}_{19}$/GGG and Pt/GGG samples, measured when the magnetic field was swept between ±90 kOe. (c) $H$ dependence of $V/(L_y \nabla T_{\mathrm{YIG}})$ in the Pt/YIG sample, measured when the magnetic field was swept between ±9 kOe. (d) Comparison between the observed $H$ dependence of $V/|V_{\mathrm{max}}|$ in the Pt/YIG sample and the $H$-$V_{\mathrm{LSSE}}$ curve calculated from Eq. (9) with $T = 300$ K and $p = 0$. Here, $V_{\mathrm{max}}$ is the maximum value of the $V$ signal. The calculation result is normalized by the $V_{\mathrm{LSSE}}$ value at $H = 1$ kOe. (e), (f) $H$ dependence of (e) $V/(L_y \nabla T_{\mathrm{YIG}})$ and (f) $V/|V_{\mathrm{max}}|$ in the Pt/YIG samples for various values of $L^z_{\mathrm{Pt}}$, measured when the magnetic field was swept between ±90 kOe. All the measurements shown in this figure were performed in the IM configuration.

The suppression of the LSSE voltage in the high magnetic field regions can be explained by the magnon gap induced by the magnetic field. Since the SSE is attributed to the spin current induced by the thermally activated magnon dynamics,[17,18,21–23,37] the suppression of magnon excitation caused by the gap opening due to the Zeeman effect[68,69] is expected to diminish the resultant ISHE voltage. In contrast, the ANE is attributed to the spin-polarized electron transport affected by the spin-orbit interaction in a ferromagnetic conductor, which is unrelated to magnon excitation. Therefore, the high field measurements provide a useful way to distinguish the LSSE from the ANE, and the observed voltage suppression under the high magnetic field confirms that the LSSE in the Pt/YIG sample is of magnon origin.

To clarify the contribution of the magnon gap to the LSSE voltage, we performed a numerical calculation. Here, we assume that the LSSE voltage $V_{\mathrm{LSSE}}$ is proportional to the following factor related to magnon excitation,[37]

$$\int_{g\mu_{\mathrm{B}}H}^{\infty} d\epsilon\; D(\epsilon,H)\epsilon^{p}[f_{\mathrm{BE}}(\epsilon,T_{\mathrm{m}}) - f_{\mathrm{BE}}(\epsilon,T_{\mathrm{e}})], \tag{8}$$

where $D(\epsilon,H) = D_0\sqrt{\epsilon - g\mu_{\mathrm{B}}H}$ is the density of states of magnons in the ferrimagnetic insulator with amplitude $D_0$, energy $\epsilon$, $g$ factor $g$, and Bohr magneton $\mu_{\mathrm{B}}$ and $p$ is an empirical factor. $f_{\mathrm{BE}}(\epsilon,T_{\mathrm{m(e)}}) = [\exp(\epsilon/k_{\mathrm{B}}T_{\mathrm{m(e)}}) - 1]^{-1}$ is the Bose-Einstein distribution function, where $k_{\mathrm{B}}$ is the Boltzmann constant and $T_{\mathrm{m(e)}}$ is the effective magnon (electron) temperature in the ferrimagnetic insulator (paramagnetic metal). By assuming that the modulation of the effective temperatures induced by the temperature gradient is very small ($T_{\mathrm{m}} \sim T_{\mathrm{e}}$ and $|T_{\mathrm{m(e)}} - T| \ll T$), we obtain

$$V_{\mathrm{LSSE}}(H,T) \propto \int_{g\mu_{\mathrm{B}}H}^{\infty} d\epsilon\; D(\epsilon,H)\epsilon^{p} \left.\frac{\partial f_{\mathrm{BE}}}{\partial T_{\mathrm{m}}}\right|_{T_{\mathrm{m}}=T}. \tag{9}$$

We numerically calculated the right-hand side of Eq. (9) and found that the observed suppression of the LSSE signal under the high magnetic field is almost reproduced by the $H$-$V_{\mathrm{LSSE}}$ curve calculated with $T = 300\,\mathrm{K}$ and $p = 0$ [Fig. 7(d)], while it cannot be explained by the simple magnon-mediated process ($p = 1$).[22,37,42] This might be due to the contribution of the phonon-mediated process,[21,37] although more detailed theoretical investigation is required for the complete understanding of the LSSE in the high magnetic field regions.

### C. Au/YIG and Au/GGG sample systems

Au is a typical metal far from the Stoner instability[50,51] and is used for the detection of the LSSE free from the proximity ANE.[33,34] However, the transverse thermoelectric voltage in the Au/YIG sample has been measured only in the IM configuration so far. In this section, we report the comparison of the thermoelectric voltage in the Au/YIG and Au/GGG samples between the IM and PM configurations.

Figure 8 shows the transverse thermopower in the Au/YIG and Au/GGG samples as a function of $H$. The Au/YIG sample in the IM configuration was found to exhibit a voltage signal reflecting the magnetization process of YIG, while only the normal Nernst voltage was observed in the PM configuration [see Figs. 8(a)–8(c)]. The contribution of the normal Nernst effect in the Au film becomes very small in the IM configuration since the high thermal conductivity of Au reduces the temperature gradient in the Au layer in the IM configuration[70] [see Eq. (6) and compare the signals in the Au/YIG and Au/GGG samples in Figs. 8(a) and 8(b)]. Notably, no ANE signal was observed in the Au/YIG sample in the PM configuration within the margin of experimental error; following the discussion in Sec. III B1, we experimentally estimate the LSSE thermopower and the proximity-ANE thermopower as $V_{\mathrm{LSSE}}/(L_y\nabla T_{\mathrm{YIG}}) = 0.080\ \mu\mathrm{V/K}$ and $V_{\mathrm{ANE}}/(L_y\nabla T_{\mathrm{YIG}}) = 0.000\ \mu\mathrm{V/K}$, respectively. Furthermore, the voltage signal in the Au/YIG sample in the IM configuration is also suppressed when the high magnetic field is applied, consistent with the behavior of the LSSE in the Pt/YIG sample [see Figs. 8(a) and 8(d)]. This result allows us to conclude again that the transverse thermoelectric voltage in the Au/YIG sample is due entirely to the LSSE and is free from the proximity ANE.

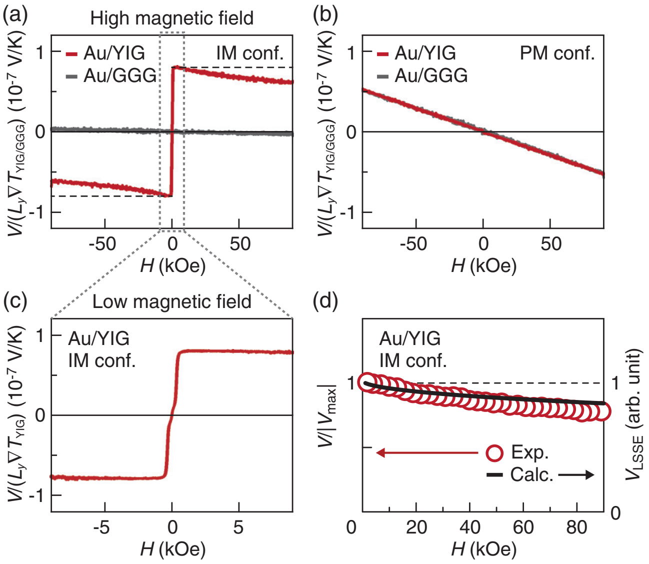

FIG. 8. (Color online) $H$ dependence of $V/(L_y\nabla T_{\mathrm{YIG/GGG}})$ in the Au/YIG and Au/GGG samples in the (a) IM and (b) PM configurations, measured when the magnetic field was swept between ±90 kOe. (c) $H$ dependence of $V/(L_y\nabla T_{\mathrm{YIG}})$ in the Au/YIG sample in the IM configuration, measured when the magnetic field was swept between ±9 kOe. (d) Comparison between the observed $H$ dependence of $V/|V_{\mathrm{max}}|$ in the Au/YIG sample and the $H$-$V_{\mathrm{LSSE}}$ curve calculated from Eq. (9) with $T = 300$ K and $p = 0$.

### D. $\mathrm{Ni_{81}Fe_{19}}$/YIG sample system

In previous sections, we have investigated the transverse thermoelectric voltage in paramagnet/ferromagnet junction systems (i.e., the Pt/YIG, Au/YIG, and $\mathrm{Ni_{81}Fe_{19}}$/GGG samples) and have shown that these samples exhibit either the LSSE or ANE. Then, what happens in a ferromagnet/ferromagnet junction system? To answer this question, in this section, we investigate the transverse thermoelectric voltage in a ferromagnetic $\mathrm{Ni_{81}Fe_{19}}$/YIG sample. If the spin current is injected into the $\mathrm{Ni_{81}Fe_{19}}$ film from the YIG slab and the ISHE appears in $\mathrm{Ni_{81}Fe_{19}}$, the hybrid thermoelectric generation based on a combination of the LSSE and ANE is expected to be realized in the $\mathrm{Ni_{81}Fe_{19}}$/YIG sample [see Fig. 9(a)].

In Fig. 9(b), we compare the transverse thermopower in the $\mathrm{Ni_{81}Fe_{19}}$/YIG and $\mathrm{Ni_{81}Fe_{19}}$/GGG samples. Although these samples exhibit a comparable ANE voltage in the PM configuration [the inset to Fig. 9(b)], the voltage signal in the $\mathrm{Ni_{81}Fe_{19}}$/YIG sample in the IM configuration was observed to be much greater than that in the $\mathrm{Ni_{81}Fe_{19}}$/GGG sample (see also Ref. 41). This voltage enhancement in the IM configuration cannot be explained by the difference in the temperature-gradient distribution between these samples, since the difference in the thermal conductivity between YIG ($\kappa_{\mathrm{YIG}} = 7.4\ \mathrm{W/mK}$) and GGG ($\kappa_{\mathrm{GGG}} = 9.0\ \mathrm{W/mK}$) is

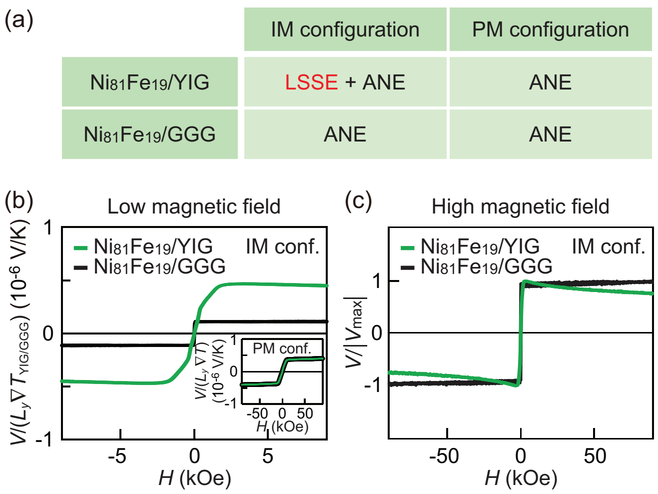

FIG. 9. (Color online) (a) LSSE and ANE in the $Ni_{81}Fe_{19}$/YIG and $Ni_{81}Fe_{19}$/GGG samples. (b) $H$ dependence of $V/(L_y \nabla T_{\mathrm{YIG/GGG}})$ in the $Ni_{81}Fe_{19}$/YIG and $Ni_{81}Fe_{19}$/GGG samples in the IM configuration, measured when the magnetic field was swept between ±9 kOe. The inset to (b) shows the $H$ dependence of $V/(L_y \nabla T_{\mathrm{YIG/GGG}})$ in the $Ni_{81}Fe_{19}$/YIG and $Ni_{81}Fe_{19}$/GGG samples in the PM configuration. (c) $H$ dependence of $V/|V_{\mathrm{max}}|$ in the $Ni_{81}Fe_{19}$/YIG and $Ni_{81}Fe_{19}$/GGG samples in the IM configuration, measured when the magnetic field was swept between ±90 kOe.

small at room temperature. Therefore, the signal difference between the $Ni_{81}Fe_{19}$/YIG and $Ni_{81}Fe_{19}$/GGG samples in the IM configuration cannot be understood if only the ANE in the $Ni_{81}Fe_{19}$ layer is taken into account.

To determine the origin of the voltage enhancement in the $Ni_{81}Fe_{19}$/YIG sample, we performed high field measurements in the IM configuration. We found that, although the ANE voltage in the $Ni_{81}Fe_{19}$/GGG sample does not change in the high magnetic field regions, the voltage signal in the $Ni_{81}Fe_{19}$/YIG sample gradually decreases with increasing the magnetic field [Fig. 9(c)], a situation similar to the LSSE signals in the Pt/YIG and Au/YIG samples. This result indicates that the enhancement of the voltage in the $Ni_{81}Fe_{19}$/YIG sample in the IM configuration is attributed to the ISHE in the $Ni_{81}Fe_{19}$ layer induced by the LSSE, and that the LSSE contribution in the $Ni_{81}Fe_{19}$/YIG sample is four times greater than the ANE contribution in the $Ni_{81}Fe_{19}$ film in the IM configuration.

## IV. SUMMARY

In this paper, we have investigated the longitudinal spin Seebeck effect (LSSE) and (normal and anomalous) Nernst effects in the Pt/$Y_3Fe_5O_{12}$ (YIG), Pt/$Gd_3Ga_5O_{12}$ (GGG), Au/YIG, Au/GGG, $Ni_{81}Fe_{19}$/YIG, and $Ni_{81}Fe_{19}$/GGG samples in in-plane magnetized (IM) and perpendicularly magnetized (PM) configurations. We have shown that a comparison of the transverse thermoelectric voltage between these configurations enables the clear separation of the LSSE from the anomalous Nernst effect (ANE) induced by static magnetic proximity. Our systematic experiments show that the Pt/YIG sample exhibits a large voltage signal only in the IM configuration, while the Pt/GGG, Au/GGG, and $Ni_{81}Fe_{19}$/GGG samples exhibit Nernst effects in both the IM and PM configurations, indicating that the thermoelectric voltage in the Pt/YIG sample is attributed to the LSSE and is not explained by the proximity ANE in the Pt layer. The possible ANE contamination in the Pt/YIG sample is experimentally estimated to be less than 0.1%, which is supported by our phenomenological model calculation. We also found that the LSSE voltage in the Pt/YIG and Au/YIG samples is suppressed by applying a high magnetic field, confirming that the mechanism of the LSSE is related to magnon excitation. Finally, we have shown that, by comparing the voltage between the IM and PM configurations, the $Ni_{81}Fe_{19}$/YIG sample enables hybrid thermoelectric generation based on the LSSE and ANE. Since the experimental methods demonstrated here provide a simple and versatile way to separate the LSSE from the ANE and to detect the pure LSSE signal, it will be useful for determining the origin of the transverse thermoelectric voltage in various metal/insulator junction systems.

## ACKNOWLEDGMENT

The authors thank Y. Tserkovnyak for valuable discussions. This work was supported by PRESTO-JST "Phase Interfaces for Highly Efficient Energy Utilization," CREST-JST "Creation of Nanosystems with Novel Functions through Process Integration," a Grant-in-Aid for Young Scientists (A) (25707029) from MEXT, Japan, a Grant-in-Aid for Scientific Research (A) (24244051) from MEXT, Japan, LC-IMR of Tohoku University, the Murata Science Foundation, the Mazda Foundation, the Sumitomo Foundation, the Tanikawa Fund Promotion of Thermal Technology, the Casio Science Promotion Foundation, and MOST (No. 2011CB921802).

---

[*] kuchida@imr.tohoku.ac.jp

[1] S. A. Wolf, D. D. Awschalom, R. A. Buhrman, J. M. Daughton, S. von Molnar, M. L. Roukes, A. Y. Chtchelkanova, and D. M. Treger, Science **294**, 1488 (2001).

[2] I. Žutić, J. Fabian, and S. Das Sarma, Rev. Mod. Phys. **76**, 323 (2004).

[3] *Concepts in Spin Electronics*, edited by S. Maekawa (Oxford University Press, Oxford, UK, 2006).

[4] G. E. W. Bauer, E. Saitoh, and B. J. van Wees, Nat. Mater. **11**, 391 (2012).

[5] *Spin Current*, edited by S. Maekawa, E. Saitoh, S. O. Valenzuela, and T. Kimura (Oxford University Press, Oxford, UK, 2012).

[6] S. Maekawa, H. Adachi, K. Uchida, J. Ieda, and E. Saitoh, J. Phys. Soc. Jpn. **82**, 102002 (2013).

[7] Y. Kajiwara, K. Harii, S. Takahashi, J. Ohe, K. Uchida, M. Mizuguchi, H. Umezawa, H. Kawai, K. Ando, K. Takanashi, S. Maekawa, and E. Saitoh, Nature (London) **464**, 262 (2010).

[8] Y. Tserkovnyak, A. Brataas, G. E. W. Bauer, and B. I. Halperin, Rev. Mod. Phys. **77**, 1375 (2005).

[9] R. H. Silsbee, A. Janossy, and P. Monod, Phys. Rev. B **19**, 4382 (1979).

[10] Y. Tserkovnyak, A. Brataas, and G. E. W. Bauer, Phys. Rev. Lett. **88**, 117601 (2002).

[11] S. Mizukami, Y. Ando, and T. Miyazaki, Phys. Rev. B **66**, 104413 (2002).
[12] A. Azevedo, L. H. Vilela Leão, R. L. Rodriguez-Suarez, A. B. Oliveira, and S. M. Rezende, J. Appl. Phys. **97**, 10C715 (2005).
[13] E. Saitoh, M. Ueda, H. Miyajima, and G. Tatara, Appl. Phys. Lett. **88**, 182509 (2006).
[14] K. Ando, S. Takahashi, J. Ieda, Y. Kajiwara, H. Nakayama, T. Yoshino, K. Harii, Y. Fujikawa, M. Matsuo, S. Maekawa, and E. Saitoh, J. Appl. Phys. **109**, 103913 (2011).
[15] K. Uchida, S. Takahashi, K. Harii, J. Ieda, W. Koshibae, K. Ando, S. Maekawa, and E. Saitoh, Nature (London) **455**, 778 (2008).
[16] K. Uchida, T. Ota, K. Harii, K. Ando, H. Nakayama, and E. Saitoh, J. Appl. Phys. **107**, 09A951 (2010).
[17] J. Xiao, G. E. W. Bauer, K. Uchida, E. Saitoh, and S. Maekawa, Phys. Rev. B **81**, 214418 (2010).
[18] K. Uchida, J. Xiao, H. Adachi, J. Ohe, S. Takahashi, J. Ieda, T. Ota, Y. Kajiwara, H. Umezawa, H. Kawai, G. E. W. Bauer, S. Maekawa, and E. Saitoh, Nat. Mater. **9**, 894 (2010).
[19] C. M. Jaworski, J. Yang, S. Mack, D. D. Awschalom, J. P. Heremans, and R. C. Myers, Nat. Mater. **9**, 898 (2010).
[20] K. Uchida, H. Adachi, T. Ota, H. Nakayama, S. Maekawa, and E. Saitoh, Appl. Phys. Lett. **97**, 172505 (2010).
[21] H. Adachi, K. Uchida, E. Saitoh, J. Ohe, S. Takahashi, and S. Maekawa, Appl. Phys. Lett. **97**, 252506 (2010).
[22] H. Adachi, J. I. Ohe, S. Takahashi, and S. Maekawa, Phys. Rev. B **83**, 094410 (2011).
[23] J. I. Ohe, H. Adachi, S. Takahashi, and S. Maekawa, Phys. Rev. B **83**, 115118 (2011).
[24] C. M. Jaworski, J. Yang, S. Mack, D. D. Awschalom, R. C. Myers, and J. P. Heremans, Phys. Rev. Lett. **106**, 186601 (2011).
[25] S. Bosu, Y. Sakuraba, K. Uchida, K. Saito, T. Ota, E. Saitoh, and K. Takanashi, Phys. Rev. B **83**, 224401 (2011).
[26] K. Uchida, H. Adachi, T. An, T. Ota, M. Toda, B. Hillebrands, S. Maekawa, and E. Saitoh, Nat. Mater. **10**, 737 (2011).
[27] M. Weiler, M. Althammer, F. D. Czeschka, H. Huebl, M. S. Wagner, M. Opel, I. M. Imort, G. Reiss, A. Thomas, R. Gross, and S. T. B. Goennenwein, Phys. Rev. Lett. **108**, 106602 (2012).
[28] K. Uchida, T. Ota, H. Adachi, J. Xiao, T. Nonaka, Y. Kajiwara, G. E. W. Bauer, S. Maekawa, and E. Saitoh, J. Appl. Phys. **111**, 103903 (2012).
[29] A. Kirihara, K. Uchida, Y. Kajiwara, M. Ishida, Y. Nakamura, T. Manako, E. Saitoh, and S. Yorozu, Nat. Mater. **11**, 686 (2012).
[30] C. M. Jaworski, R. C. Myers, E. Johnston-Halperin, and J. P. Heremans, Nature (London) **487**, 210 (2012).
[31] S. S.-L. Zhang and S. Zhang, Phys. Rev. B **86**, 214424 (2012).
[32] Y. Ohnuma, H. Adachi, E. Saitoh, and S. Maekawa, Phys. Rev. B **87**, 014423 (2013).
[33] D. Qu, S. Y. Huang, J. Hu, R. Wu, and C. L. Chien, Phys. Rev. Lett. **110**, 067206 (2013).
[34] T. Kikkawa, K. Uchida, Y. Shiomi, Z. Qiu, D. Hou, D. Tian, H. Nakayama, X.-F. Jin, and E. Saitoh, Phys. Rev. Lett. **110**, 067207 (2013).
[35] D. Meier, T. Kuschel, L. Shen, A. Gupta, T. Kikkawa, K. Uchida, E. Saitoh, J.-M. Schmalhorst, and G. Reiss, Phys. Rev. B **87**, 054421 (2013).
[36] R. Ramos, T. Kikkawa, K. Uchida, H. Adachi, I. Lucas, M. H. Aguirre, P. Algarabel, L. Morellón, S. Maekawa, E. Saitoh, and M. R. Ibarra, Appl. Phys. Lett. **102**, 072413 (2013).
[37] H. Adachi, K. Uchida, E. Saitoh, and S. Maekawa, Rep. Prog. Phys. **76**, 036501 (2013).
[38] K. Uchida, T. Nonaka, T. Kikkawa, Y. Kajiwara, and E. Saitoh, Phys. Rev. B **87**, 104412 (2013).
[39] K. S. Tikhonov, J. Sinova, and A. M. Finkel'stein, Nat. Commun. **4**, 1945 (2013).
[40] H. Adachi and S. Maekawa, J. Korean Phys. Soc. **62**, 1753 (2013).
[41] B. F. Miao, S. Y. Huang, D. Qu, and C. L. Chien, Phys. Rev. Lett. **111**, 066602 (2013).
[42] S. Hoffman, K. Sato, and Y. Tserkovnyak, Phys. Rev. B **88**, 064408 (2013).
[43] M. Schreier, A. Kamra, M. Weiler, J. Xiao, G. E. W. Bauer, R. Gross, and S. T. B. Goennenwein, Phys. Rev. B **88**, 094410 (2013).
[44] Y.-T. Chen, S. Takahashi, H. Nakayama, M. Althammer, S. T. B. Goennenwein, E. Saitoh, and G. E. W. Bauer, Phys. Rev. B **87**, 144411 (2013).
[45] H. Nakayama, M. Althammer, Y.-T. Chen, K. Uchida, Y. Kajiwara, D. Kikuchi, T. Ohtani, S. Geprägs, M. Opel, S. Takahashi, R. Gross, G. E. W. Bauer, S. T. B. Goennenwein, and E. Saitoh, Phys. Rev. Lett. **110**, 206601 (2013).
[46] C. Hahn, G. de Loubens, O. Klein, M. Viret, V. V. Naletov, and J. Ben Youssef, Phys. Rev. B **87**, 174417 (2013).
[47] N. Vlietstra, J. Shan, V. Castel, B. J. van Wees, and J. Ben Youssef, Phys. Rev. B **87**, 184421 (2013).
[48] M. Althammer, S. Meyer, H. Nakayama, M. Schreier, S. Altmannshofer, M. Weiler, H. Huebl, S. Geprägs, M. Opel, R. Gross, D. Meier, C. Klewe, T. Kuschel, J.-M. Schmalhorst, G. Reiss, L. Shen, A. Gupta, Y.-T. Chen, G. E. W. Bauer, E. Saitoh, and S. T. B. Goennenwein, Phys. Rev. B **87**, 224401 (2013).
[49] N. Vlietstra, J. Shan, V. Castel, J. Ben Youssef, G. E. W. Bauer, and B. J. van Wees, Appl. Phys. Lett. **103**, 032401 (2013).
[50] H. Ibach and H. Lüth, *Solid-State Physics: An Introduction to Principles of Materials Science* (Springer, Berlin, 2009).
[51] D. A. Papaconstantopoulos, *Handbook of the Band Structure of Elemental Solids* (Plenum, New York, 1986).
[52] S. Y. Huang, X. Fan, D. Qu, Y. P. Chen, W. G. Wang, J. Wu, T. Y. Chen, J. Q. Xiao, and C. L. Chien, Phys. Rev. Lett. **109**, 107204 (2012).
[53] S. Geprägs, S. Meyer, S. Altmannshofer, M. Opel, F. Wilhelm, A. Rogalev, R. Gross, and S. T. B. Goennenwein, Appl. Phys. Lett. **101**, 262407 (2012).
[54] Y. M. Lu, Y. Choi, C. M. Ortega, X. M. Cheng, J. W. Cai, S. Y. Huang, L. Sun, and C. L. Chien, Phys. Rev. Lett. **110**, 147207 (2013).
[55] S. O. Valenzuela and M. Tinkham, Nature (London) **442**, 176 (2006).
[56] T. Kimura, Y. Otani, T. Sato, S. Takahashi, and S. Maekawa, Phys. Rev. Lett. **98**, 156601 (2007).
[57] W. Nernst, Ann. Phys. (Leipzig) **267**, 760 (1887).
[58] L. Berger, Phys. Rev. B **5**, 1862 (1972).
[59] T. Miyasato, N. Abe, T. Fujii, A. Asamitsu, S. Onoda, Y. Onose, N. Nagaosa, and Y. Tokura, Phys. Rev. Lett. **99**, 086602 (2007).
[60] S. Y. Huang, W. G. Wang, S. F. Lee, J. Kwo, and C. L. Chien, Phys. Rev. Lett. **107**, 216604 (2011).
[61] M. Mizuguchi, S. Ohata, K. Uchida, E. Saitoh, and K. Takanashi, Appl. Phys. Express **5**, 093002 (2012).

[62] Y. Sakuraba, K. Hasegawa, M. Mizuguchi, T. Kubota, S. Mizukami, T. Miyazaki, and K. Takanashi, Appl. Phys. Express **6**, 033003 (2013).

[63] J. Flipse, F. L. Bakker, A. Slachter, F. K. Dejene, and B. J. van Wees, Nat. Nanotechnol. **7**, 166 (2012).

[64] G. A. Slack and D. W. Oliver, Phys. Rev. B **4**, 592 (1971).

[65] H. Nakayama, K. Ando, K. Harii, T. Yoshino, R. Takahashi, Y. Kajiwara, K. Uchida, Y. Fujikawa, and E. Saitoh, Phys. Rev. B **85**, 144408 (2012).

[66] Y. Sun, H. Chang, M. Kabatek, Y. Y. Song, Z. Wang, M. Jantz, W. Schneider, M. Wu, E. Montoya, B. Kardasz, B. Heinrich, S. G. E. te Velthuis, H. Schultheiss, and A. Hoffmann, Phys. Rev. Lett. **111**, 106601 (2013).

[67] Y. Liu, T. A. George, R. Skomski, and D. J. Sellmyer, Appl. Phys. Lett. **99**, 172504 (2011).

[68] Y. Onose, T. Ideue, H. Katsura, Y. Shiomi, N. Nagaosa, and Y. Tokura, Science **329**, 297 (2010).

[69] A. L. Chernyshev, Phys. Rev. B **86**, 060401(R) (2012).

[70] A. Slachter, F. L. Bakker, and B. J. van Wees, Phys. Rev. B **84**, 020412(R) (2011).